A 2 DEGREE-OF-FREEDOM SOI-MEMS TRANSLATION STAGE WITH CLOSED LOOP POSITIONING

BY

BONJIN KOO

THESIS

Submitted in partial fulfillment of the requirements
for the degree of Master of Science in Mechanical Engineering
in the Graduate College of the
University of Illinois at Urbana-Champaign, 2014

Urbana, Illinois

Adviser:

Tungchao Julia Lu Professor Placid M. Ferreira

ABSTRACT

This research contains the design, analysis, fabrication, and characterization of a closed loop XY micro positioning stage. The XY micro positioning stage is developed by adapting parallel-kinematic mechanisms, which have been widely used for macro and meso scale positioning systems, to silicon-based micropositioner. Two orthogonal electrostatic comb drives are connected to moving table through 4-bar mechanism and independent hinges which restrict unwanted rotation in 2-degree-of-freedom translational stage. The XY micro positioning stage is fabricated on SOI wafer with three photolithography patterning processes followed by series of DRIE etching and HF etching to remove buried oxide layer to release the end-effector of the device. The fabricated XY micro positioning stage is shown in Fig1 with SEM images. The device provides a motion range of 20 microns in each direction at the driving voltage of 100V. The resonant frequency of the XY stage under ambient conditions is 811 Hz with a high quality factor of 40 achieved from parallel kinematics. The positioning loop is closed using a COTS capacitance-to-voltage conversion IC and a PID controller built in D-space is used to control position with an uncertainty characterized by a standard distribution of 5.24nm and a approximate closed-loop bandwidth of 27Hz. With the positioning loop, the rise time and settling time for closed-loop system are 50ms and 100ms. With sinusoidal input of ω=1Hz, the maximum phase difference of 108nm from reference input is obtained with total motion range of 8μm.

ACKNOWLEDGMENTS

I would like to thank Prof. Placid M. Ferreira for guiding and supporting my research with mentorship and encouragement throughout my studies at University of Illinois at Urbana-Champaign. I am also grateful to Prof. Srinivasa Salapaka for letting me use his laboratory equipments and providing valuable advices on my research. Additionally, I appreciate Prof. Jingyan Dong for working together on designing fabrication processes and experimental setup.

I would also like to thank the support staff of all the cleanrooms that I have worked in for my research, including Michael R. Hansen, Glennys A. Mensing, Edmund Chow, and Yaguang Lian.

Lastly, I would like to acknowledge my family for endless love, sacrifices and prayers.

TABLE OF CONTENTS

CHAPTER 1

INTRODUCTION

Multi-axis positioning with high performance is critical to modern micro/nano manipulation and manufacturing technologies. Micro/nano positioning with high bandwidth along with high accuracy and precision can improve performance in micro-machining, micro-assembly, and lithography processes. It can also be used in many applications such as fiber optical switches [1], micro-force sensors [2,3], scanning probe microscopy [4, 5], imaging and data storage [6-8], micro optical lens scanner[9-12]. For these applications, size, motion range, natural frequency and cross-coupling of motion along the different degrees of freedom are the most important characteristics that are directly related to a system's performance. MEMS-scale positioning devices can play an important role in many of these situations. As primary positioning systems, they can reduce the overall system size or, as secondary positioning systems, they can provide a fine positioning/adjustment capability very close to the functional element of the system. The size of a micro positioning device can reduce stack-up and assembly errors. It can also decrease vulnerability to environmental changes. Thermal or gravitational effects become very small compared to range of motion in system and can be neglected. Further, the associated decrease in mass as the size of the system decreases greatly improves its dynamic performance.

Motivated by these applications and considerations many MEMS-scale stages were introduced and developed. Previous research efforts in stage development [2, 3] has led to stages that directly connect two orthogonal combs to the moving table to generate X and Y displacement. Such designs result in very small workspaces and produce side instabilities due to the gap changes between comb fingers that result from cross talk between the two axes of motion.

The widely-used XY stage design [5, 6, 8, 10, 13-15] uses four identical comb actuators arranged around the end-effector, each perpendicular to its neighbor, and connected to the moving table by long slender beams. When the stage is actuated in the X direction, the beam along the Y direction acts as a leaf spring to accommodate the motion of the X axis and vice versa. The cross-talk between the axes is decreased by reducing the stiffness of these beams. The net result, however, is non-determinism in the motion produced (especially when resisting forces are present) and an inability to arrest rotations. Further, the reduced stiffness leads to lower resonant frequencies and complex dynamics [16] with multiple modes in a fairly narrow frequency band. Serial kinematic linkage designs [11, 12] realize two degrees of freedom by serial conjugation of single DOF systems. In these designs, one stage (called the inner stage) is embedded into the moving part of the other (outer) stage. The actuation of the outer stage moves the entire inner stage with the actuator of the inner stage producing a motion in a direction orthogonal to that produced by the outer stage. Thus, the end-effector, carried by the inner stage, can be moved in both, the X and Y, directions. Notwithstanding the difficulties of fabricating such a system and electrical isolation problems associated with electrical connections the inner stage, an additional disadvantage of this design is that inertial load of the outer axis is significantly larger than of the inner axis, causing a decrease the natural frequency and response time of the outer axis and mismatched dynamics between the two axes of motions.

1.1 Design Configuration (SKM and PKM)

Among all the factors involved in the design of stage, choosing or designing its kinematic configuration is possibly the most important. Positioning systems may broadly be categorized as having serial or parallel kinematics. Serial Kinematic Mechanisms (SKM) has open kinematics chains. They are composed of motion axes connected serially from a fixed base to the

end-effector. They are easy to design, fabricate and assemble but they tend to have large inertia, low overall stiffness. As a result they exhibit poor dynamic performance and low bandwidth. Because of the serial connectivity of the motion axes of the mechanism, the workspace of such system is large. Parallel Kinematic Mechanisms (PKM), truss-like structures, give such systems high rigidity, potentially low mass, and improve dynamic performance. The price paid, however, is in the size of the workspace and the complex, typically non-linear relation between the motions of the controlled axes/joints and the end-effector of the system to a fixed base.

1.2 Parallel Kinematic Mechanism (PKM) for Micro Positioning Stage

The PKM is suitable for developments of micro/nano positioning stages because it has advantages over SKM, such as lower inertia, smaller package size and higher stiffness. Therefore PKM stages have their potential for high performance in resolution, reliability, and rigidity. It also satisfies the needs for good dynamic performance with high bandwidth. Unlike SKM, the moving axis in PKM does not have to carry the weight of other linkages and drives and therefore the effective mass of the system decreases. PKMs can be designed so that all the drives/actuators are located on the fixed link (ground). This is greatly decreases the inertia and makes interconnect to the drives simple. The smaller inertia of system eventually leads to better dynamic performances. On the other hand, PKM has drawbacks in dexterity, workspace, and non-linearity. Because of the kinematic conditions and singularities, the effective workspace is limited for PKM devices. Similarly, non-linearity from certain conditions in Jacobian matrix limits the system performances. Also, analyzing kinematic and dynamic parameters using multiple linkages between fixed base and end-effector is difficult.

1.3 Previous Researches in MEMS Positioning Stages

Our research, therefore, has concentrated on adapting parallel kinematic systems, which have been widely used for macro and meso scale positioning systems [17-19, 23], to silicon-based MEMS-scale micropositioners. A Parallel Kinematic Mechanism (PKM) consists of a fixed base and movable end-effector connected, in parallel, by multiple independent kinematic chains, each constraining the end-effector along one or more DOF while accommodating or admitting displacements along the its remaining DOFs. Together, these chains restrict all undesired motions (for example, all rotations for a translational stage) and map the desired DOFs to the actuated/controlled joints of the kinematic chains. In this way, a mechanism is realized in which the desired DOFs are spanned by the actuators and the undesired DOFs are restricted by the interaction of the kinematic chains. Parallel kinematic mechanisms generally produce high structural stiffness because of their truss-like structures resulting in higher natural frequencies, and when appropriately designed, can result in configurations where near complete decoupling of the actuation is achieved. PKMs are criticized for the small workspaces or motion ranges because the motion is restricted to the intersection of the motion range of all its kinematics chains. While a valid criticism for macro-scale systems, where the kinematic joints and actuators have large permissible motion ranges, for MEMS stage designs in which the motion range of the stage is more likely to be governed by the limits of the actuators and flexure joints than the mechanism itself, this is not an issue.

In the past, our work has introduced electrostatically-driven, MEMS-scale, parallelogram 4-bar stage designs and used both, linear and rotary combs to actuate them [20, 21], demonstrating de-coupled XY motion of about 20 microns with stage bandwidths of about 1 kHz and Q-factors of about 100; three degree-of-freedom stages with two translations and one

rotation (XYθ); stages with tilt-plate actuated cantilevers for XY&Z motion [20]; and approaches to actuating and sensing on using a single comb structure [22]. These devices were all operated in open-loop without any feedback signal on displacement, which was sufficient for applications that did not require precise positioning.

1.4 The Scope of This Work

In this thesis, motivated by applications such as tissue and cell testing in mechanobiology and scanned probe imaging, we address the closed-loop control of the axes of the stages. The thesis provides the explanations of the redesign of stage, modification of fabrication steps, tests and characterization of sensing elements, and experimental results using closed-loop control. Chapter 2 summarizes the redesign of stage for closed-loop operations. Sensing combs, added to each axis of the stage, consisting of a parallelogram 4-bar linkage connecting end-effector with a linear comb drive actuator, are designed to work with an inexpensive COTS capacitance-to-voltage conversion to affect a closed-loop XY positioning stage. Chapter 3 provides an overview of modified fabrication steps using typical micro fabrication processes such as photolithography, sputtering, lift-off, wet etching, and dry etching. Chapter 4 presents the characterization of the sensing combs and the open loop behaviour of the stage. Chapter 5 describes the closed loop performance of the system and Chapter 6 draws up conclusions and recommendations for future work.

CHAPTER 2

DESIGN OF AN XY MEMS STAGE WITH MOTION SENSING

2.1 Design of parallel kinematics (4-bar mechanisms)

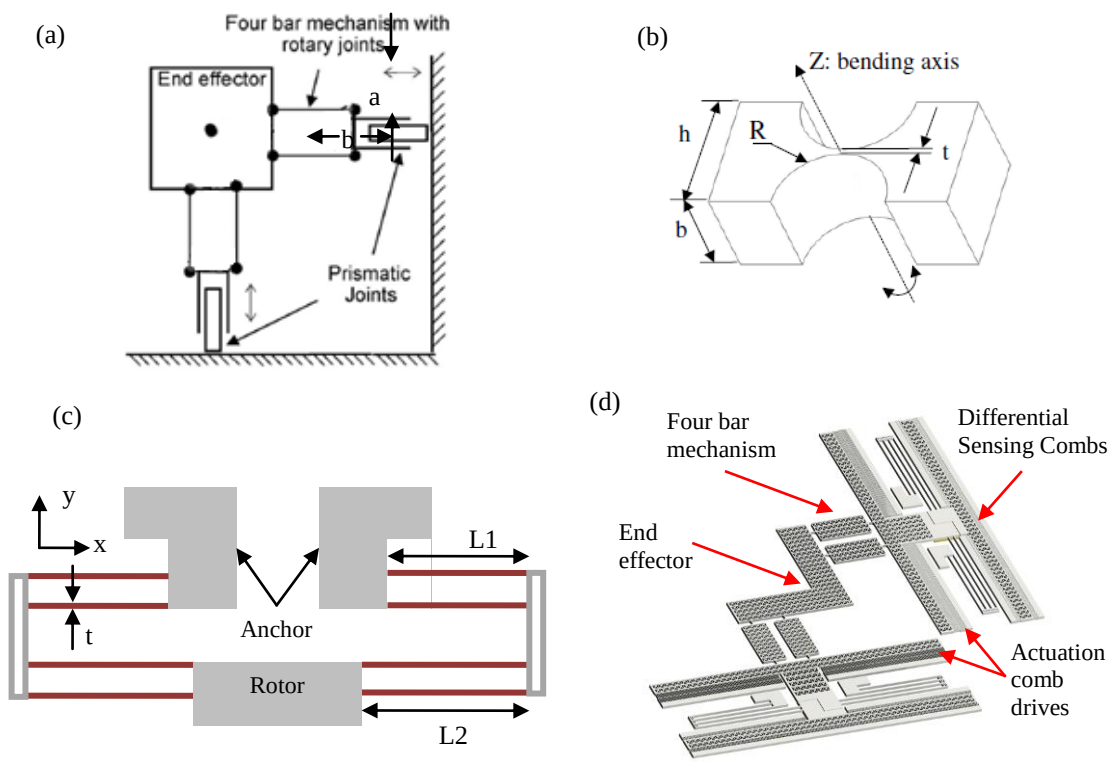

Fig. 2.1. Schematic diagram of XY micro positioning stage. (a) Kinematic model for XY micro stage (b) Single-axis flexure hinge (c) Leaf spring (d) Solid model for XY micro stage

The basis of the stage design is a variation of a parallel-kinematic scheme [20] that has been successfully been adapted for MEMS-scale devices driven by linear electrostatic combs [20, 21, 22]. A solid model of the stage, along with its kinematic scheme is shown in Fig. 2.1.(d). The end-effector or table is connected to the base by two kinematic chains, each consisting of freely mobile 4-bar parallelogram linkage mechanisms carried by a controlled prismatic joint. The two

prismatic joints provide the independent controlled displacements in the X and Y directions while the freely mobile 4-bar system in each kinematic chain provides it with the degree of freedom to accommodate the controlled motion of the other. Kinematically, the table is the connector for the two 4-bar linkages and, because of the parallelogram geometry of the 4-bar mechanisms, it does not undergo any rotation. Thus, a 2 degree-of-freedom, planar translator is obtained. For the MEMS-scale stage, the controlled prismatic joint is physically realized by a linear comb electrostatic drive mounted on a leaf spring, while the 4-bar mechanism is realized by connecting rigid members by flexure hinges as shown in Fig. 2.1.(d). The second pair of linear combs in the system are sensing combs designed to enable feedback control of the system. It is important to note that, for the range of motion desired in such MEMS-scale systems, these designs have been found to produce linear, decoupled, orthogonal motion.

Detailed kinematic and dynamic analyses as well as the rationale for designing components of the stage have been previously reported [20, 21]. Here, we use the same approaches and design and refer the reader to those references for additional details. The stage is designed for a fabrication on an SOI wafer, with a heavily doped 50 micron device layer, a 500 micron handle layer and a 2 micron BOX layer. The leaf springs (design shown in Fig. 1(d)) have been designed with dimensions of L1=1.38mm and L2=1.90mm and leaf thickness of 8 μm, to obtain spring constants for the X direction and Y direction, i.e. kx and ky, is 1.85 N/m and ~83,000 N/m respectively. Therefore the ratio of two stiffness, ky/kx, is ~45,000. All rotational hinges (See Fig. 2.1.(b)) are designed with thickness t = 6 μm, R = 300 μm, h = 70 μm and b = 50 μm, to produce a stiffness and maximum rotation range (based on the yield limit) of 3.1 × 10–6 N m rad–1 and 0.68 rad, respectively. The length of the parallelogram 4-bar links is 1 mm, thus allowing a maximum 630 μm displacement of the 4-bar mechanism. Factors such as the

maximum displacement of the comb drives predominantly determine the maximum displacement of each axis.

2.2. Design of actuators

The actuation combs are designed with 188 fingers and 50μm finger height (device layer thickness), 5μm finger spacing, and 10μm nominal overlap. They are designed to produce electrostatic force that is sufficient to overcome the resistance of folded spring and flexure hinges to produce the desired motion at a designed maximum actuation voltage. The electrostatic force, given by $F = n\frac{\varepsilon_0 h V^2}{g}$, where n is the number of finger pairs (= 188), h is the height of a finger (50 μm), g is the gap between two neighbouring fingers (5 μm), and ε_0 is the electrical permittivity of air, is 81.5 μN at 70V. This force, given the designed stiffness of the leaf and rotational springs and the kinematics of the mechanism, produces a displacement of 22μm.

2.3. Modal analysis

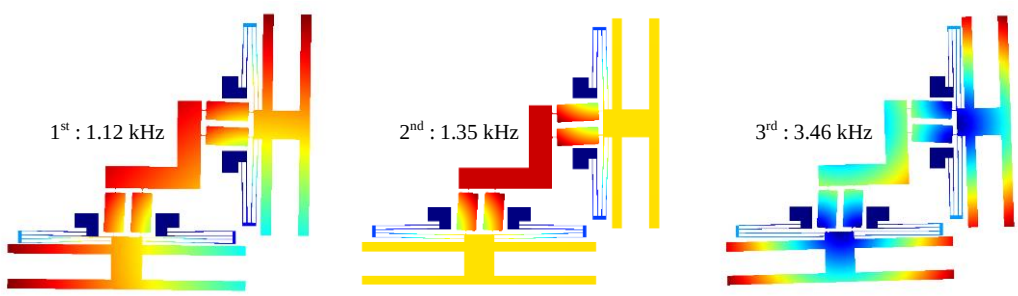

Fig. 2.2. Mechanical natural frequencies without damping condition and corresponding modal shapes in XY-plane.

Modal analysis is performed by COMSOL finite element analysis (FEA) software on the device to estimate its dynamic responses. Fig. 2.2 shows the results of this analysis, suggesting that the first two modes are pure translations along the (1,1) and (-1,1) directions (i.e., with the

leaf springs in anti-phase and in-phase deflection) with associated modal frequencies of 1.12 and 1.35 kHz. The next mode is a rotational mode with a modal frequency of 3.46 kHz and therefore around 10 times stiffer than the translational modes.

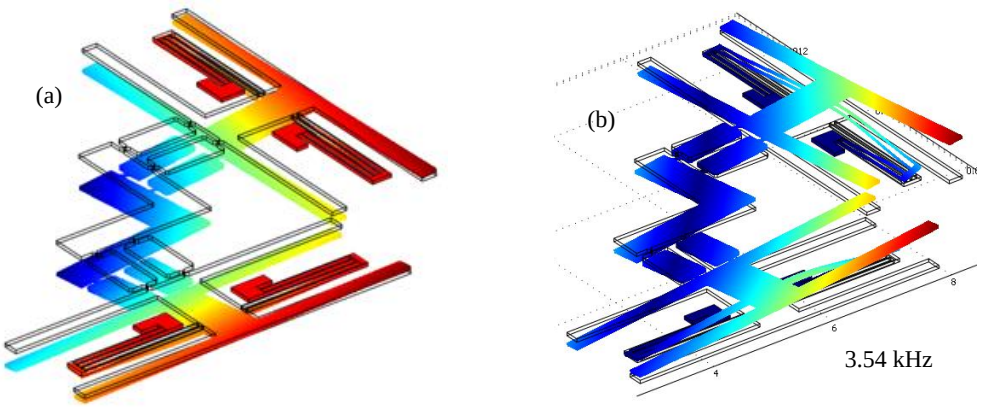

Fig. 2.3. (a) Maximum device deflection under self weight less than 20nm.
(b) Model shape and natural frequencies of the dominant Z-mode. .

Out-of-plane sagging of the stage due to its own weight can lead to the twisting of the leaf springs, misalignment between the comb fingers affect the orientation of the stage, and introduce additional stresses at the hinges. A surface load corresponding to the weight of the structure is applied to the top surface of the device. Finite element analysis (FEA) shows that the sagging effect of the stage under self-weight is negligible (less than 20nm at the comb drives) when compared with the overall dimension of the device. From 3-D FEA, the dominant mode in z direction is about 3.54 kHz, as shown in Fig. 2.3, The XY modes from 3D analysis are similar to that from 2D simulation. Since Z-mode is much stiffer than XY-modes and actuation is along XY-axis, the out-of-plane motion is negligible for this device.

2.4. Design of sensors and controllers

The stage has built-in differential capacitance sensing combs for each axis. They produce a capacitance change that is proportional to the displacement of the axis and sensed by a capacitance-to-voltage chip, the MS3110 Universal Capacitive Readout IC. The voltage generated by the IC is used as the feedback signal for the closed-loop control of the device. The chip has a resolution of 4.0aF/√Hz and a range up to 10pF. The differential capacitance comb sensing system is made up of two opposed combs so that motion of the axis reduces the finger overlap (and hence, capacitance) for one comb while increasing that increasing that for the other. The first, SENS1 has 188 fingers while the second, SENS2 has 156 fingers. Each finger has a height of 50 μm (the thickness of the SOI device layer) with a gap of 5μm between the adjacent fingers. The initial overlap between the moving and stationary fingers for SENS1 and SENS2 are 30μm and 10μm respectively. With an actuation voltage of 70V, the finger overlaps of the two sensing combs changes by 10μm, corresponding to theoretical differential change in capacitance of 0.305pF. Therefore, the sensing comb produces a capacitive change rate, $\Delta C/\Delta x$, of 0.0305pF/μm with air being the medium between the comb fingers.

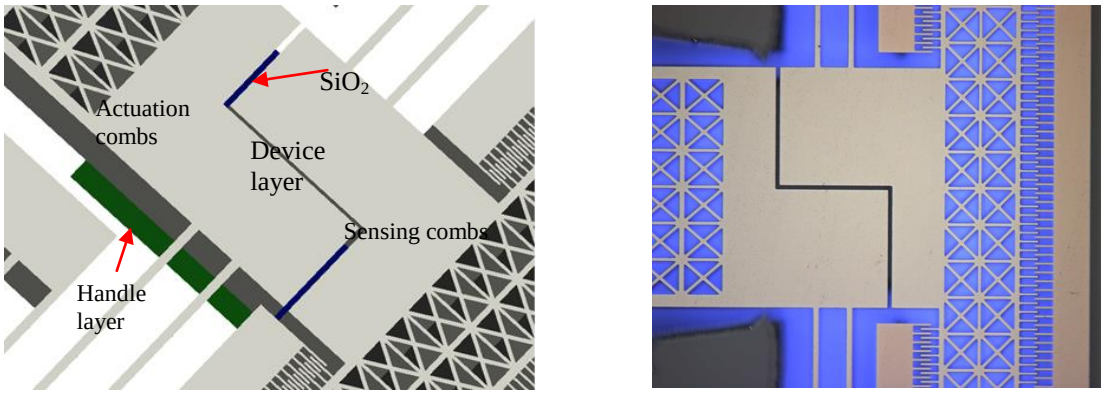

Fig. 2.4. 3D schematic model demonstrate the isolation of the for XY stage near isolated device layer

The device presented in this paper has an actuation comb and a differential sensing comb

designed for each axis. The electrical isolation between the actuation comb drive and sensing comb drive is very important for the achievable performance of the closed-loop control. If the actuating combs and the sensing combs are electrically connected together, it will impose an impediment in circuit design since the actuator requires high actuation voltage (typically more than 50 V) while the sensing signal usually is less than 5V. To reduce the interference between actuation and sensing circuits, in our device design, the sensing and the actuation combs are mechanically separated and electrically disconnected in the device layer, but are mechanically jointed together by an underlining connection pad that is composed of the insulation SiO2 (buried oxide) layer and partially etched handle layer silicon, as shown in Fig.2.4. The thickness of the handle layer silicon in the connection pad is controlled by etching retardation, so as to minimize the weight from the connection pad.

A dSPACE (DS1104) controller with analog voltage input/output channels are used to receive the sensing displacement signal and provide the actuation command. The output of the sensor is fed into the dSPACE controller through a 16-bit D/A converter which has a resolution of 76.29μV. With the MS3110 IC's resolution of 4.0aF/√Hz, a theoretical capacitance sensing resolution and positioning resolution can be calculated and they are 1.05E-5pF and 0.64 nanometers respectively.

CHAPTER 3

FABRICATION OF XY MEMS STAGE

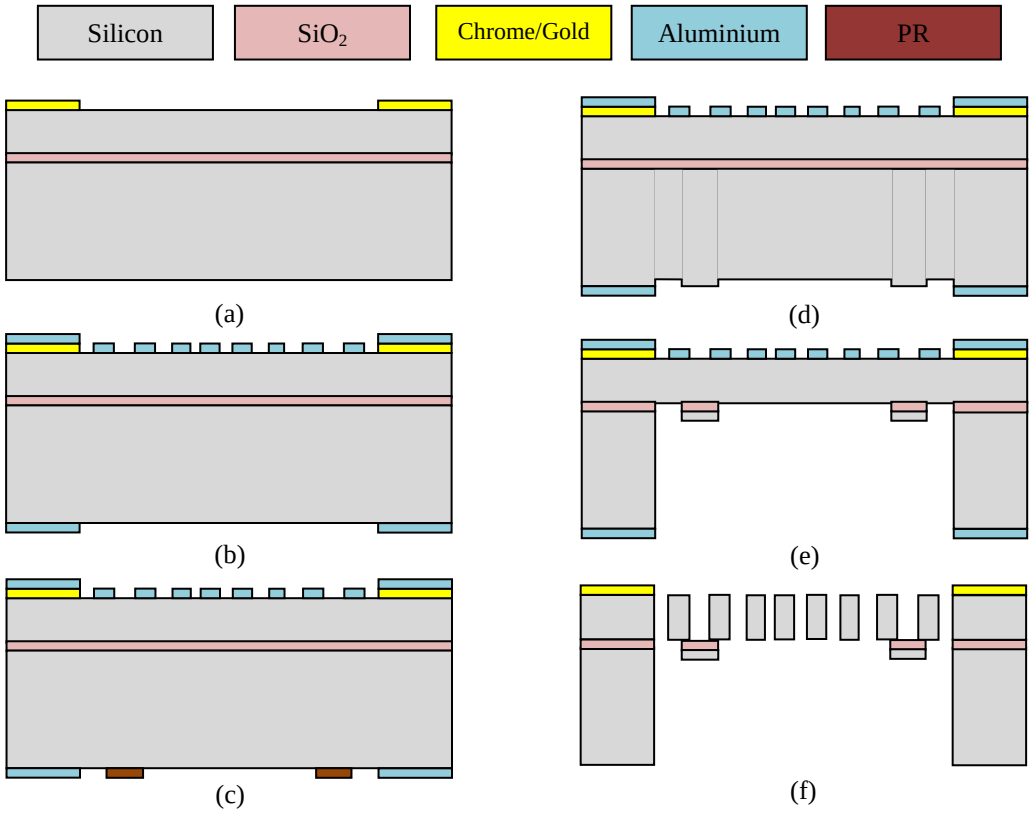

Fig. 3.1. Cross section views for process flow. (a) Chrome/Gold .deposition to create electrodes to comb drive; (b) Top-side/bottom-side aluminium mask patterning; (c) PR retardation layer patterning. (d) DRIE of bottom-side silicon(create retardation layer); (e) Complete DRIE and HF etching to remove oxide layer; (f) DRIE of top-side silicon followed by aluminium mask etch

The overall fabrication procedure for MEMS XY positioning stage is summarized in Fig. 3.1. The stage is fabricated in a SOI wafer with 50μm of p-doped device layer and 500 μm handle in four photolithography patterning steps; two top-side patterning steps (one for patterning the actual device and one for the chrome/gold electrodes) and two bottom-side patterning steps (one

for patterning handle layer cavity, and one for patterning connection pads with etching retardation). The retardation layer is a PR mask that is used to make mechanical connection (~70 μm thick) pad. During the long DRIE process for etching the handle layer silicon, with the retardation PR, a 70 μm thick pad structure is left on the handle layer silicon.

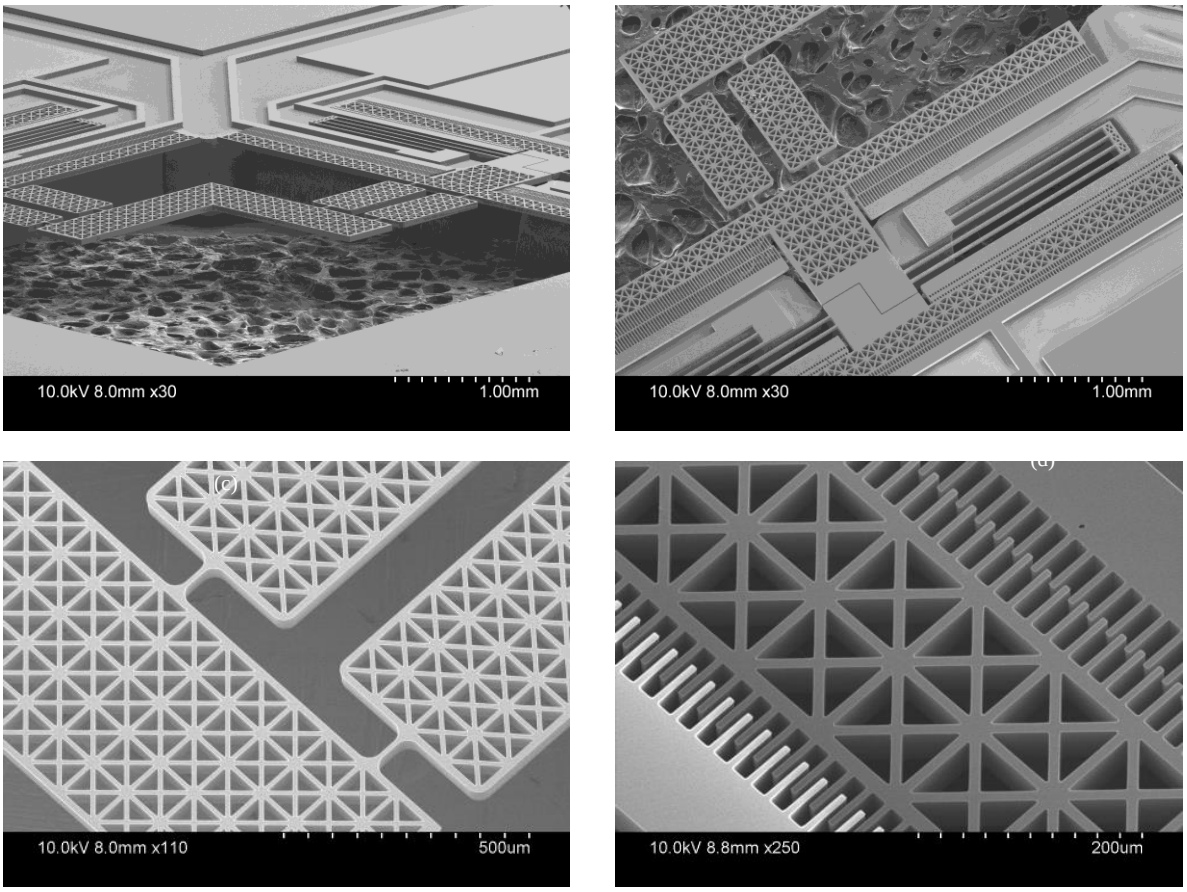

Fig. 3.2. SEM pictures for micropositioning XY stage. (a) Overall structure; (b) Isolation between actuation and sensing comb drives; (c) Hinges (d) Differential comb drives for sensing.

During the fabrication, the gold/chrome electrodes are first patterned. Using the electrode features for alignment, the device pattern including the comb drives, folded spring, flexure hinges and end effector are transferred to an aluminium film on the device layer of the die using standard lift-off processes. Next bottom-side patterns for cavity and retardation layer are transferred to handle layer in order and DRIE is used to open up a large cavity below the device

with 70μm thick connector shown in Fig. 3.1. This is followed by an HF (hydrofluoric) acid etch to remove the now-exposed buried oxide layer in the cavity. DRIE is repeated on the top-side to complete and release the device. Finally, the aluminium mask used for top-side and bottom-side pattern is etched away. Fig. 3.2 shows the results of the fabricated device.

CHAPTER 4

CALIBRATION AND EXPERIMENTAL SETUP

The fabricated device performance is first checked with LCR meter (Agilent 4284A) to verify that a change of capacitance is detectable at the combs. For each axis of the stage, the capacitance of each sensing comb drive is recorded by the LCR meter while it is also being driven by a voltage bias, swept from -40V to 40V with step increases of 0.5V. Fig. 4.1 shows data for five consecutive voltage sweep measurements on one of the sensing combs of the stage, indicating that a clearly measurable displacement signal is possible using the MS3110 chip. Additionally, notable information from LCR meter is that the initial parasitic capacitances associated with the combs is relatively high due larger domains of doped silicon associated with

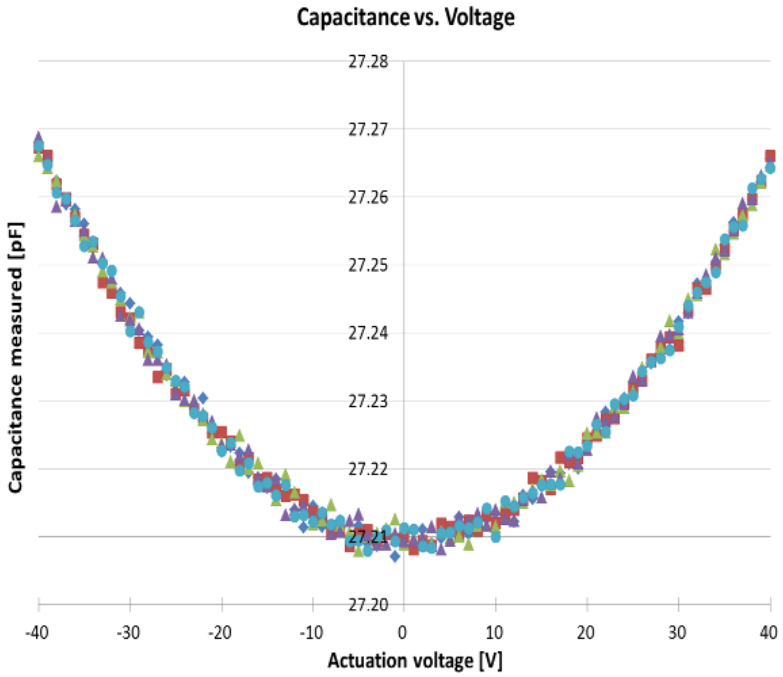

Fig. 4.1. Sensing comb calibration with LCR meter

the routing of contacts to the device and the relatively large test pads, leads and probe contact. Because of small working capacitance range of MS3110 sensor, the sensing circuit is designed to work in a differential mode to accommodate this large parasitic capacitance.

The actuator combs are characterized by measuring the static displacement as a function of the driving voltage. To do this, each actuation comb is driven by a power supply (Keithley 237) and the displacement of the comb is observed by tracking a feature on the end-effector using a high resolution (1 micron) optical microscope as the actuation voltage is increased in steps of 5V to maximum of 100V and then decreased by the same steps back to zero. Fig. 4.1 shows displacement as a function of diving voltage at the x and y axes actuation combs. The typical second-order voltage-displacement characteristics are observed.

4.1 Circuit description

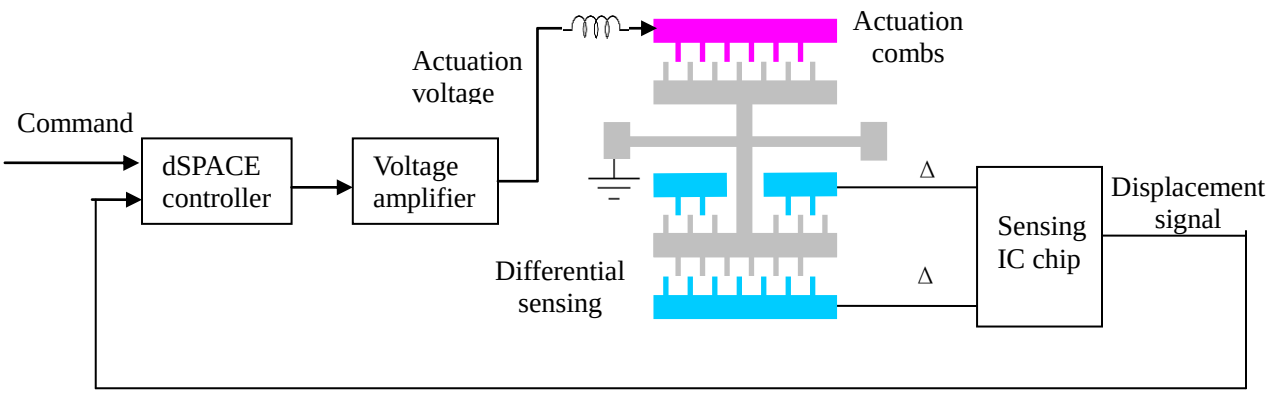

Fig. 4.2. Circuit diagram for the actuation and sensing needed for control implementation

Fig. 4.2 shows the circuit schematic for displacement measurement circuit with the sensing combs connected to the MS3110 IC. The IC is powered by a battery cell in order to reduce the effects of the line noise on the measurements. It is operated in a differential capacitance mode (CS2-CS1) with CS2 connected to sensing comb SEN1 and CS1 connected to sensing comb

SEN2 with a tuneable capacitor connected in parallel. The tuneable capacitor is used to balance the difference between the two sensing comb drives so that the overall capacitance is in proper range (0.5pF ~ 10pF) for the sensor, as shown in Fig. 4.2.

4.2 Calibration from capacitance to displacement

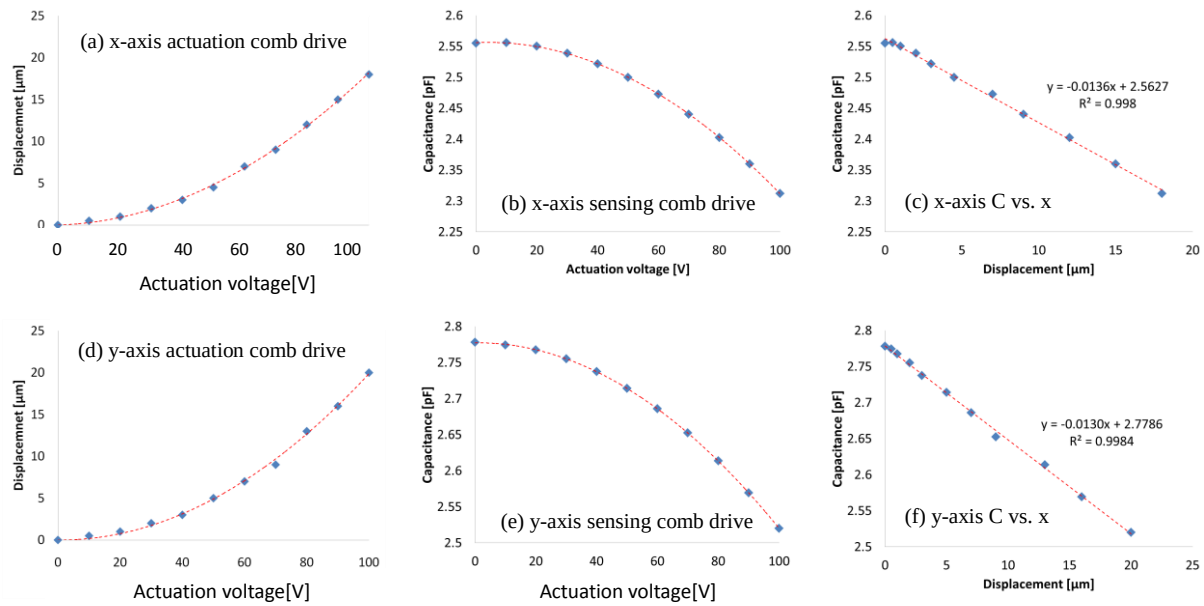

Fig. 4.3. Calibration of actuation comb drives and sensing comb drives

Fig. 4.3(b) shows the capacitance readings at the sensing combs of the X axis of the stage for different voltages at the actuation comb. The results from Y-axis follow a similar behaviour. The information from displacement test in Figure 4.3(a) is integrated with capacitive measurement test to produce the capacitance-displacement characteristics for the axis, given in Fig. 4.3(c). For the entire displacement range, it can be observed that the characteristics are linear as one would expect, producing a sensitivity of 0.0136pF/micron for x-axis and 0.0130pF/micron for y-axis. With a conversion gain of 5.5347 volts/pF and a 16 bit D/A converter, one can expect a displacement resolution of 1.01nm for x-axis and 1.06nm for y-axis with this system. Note that

the experimental values for sensitivity of the x and y-axis combs are only 45% and 43% of theoretical value of 0.0305pF/μm, expected from the comb design. This discrepancy is mainly caused by finger gap variation caused by undercutting during DRIE fabrication process as shown in Fig. 4.4. A SEM picture of the comb fingers was taken right after the DRIE process. A undercutting can be observed between the Al mask and the underneath actual silicon structure below Al mask. The actual gap for the fabricated device was measured to be 9μm in SEM micrographs, while the designed value is 5μm. This reduces the expected sensitivity ($\Delta C/\Delta x$) to 0.0169pF/ μm. With this adjustment, the measured sensitivities for x-axis and y-axis are a more reasonable 80% and 77% of expected value respectively.

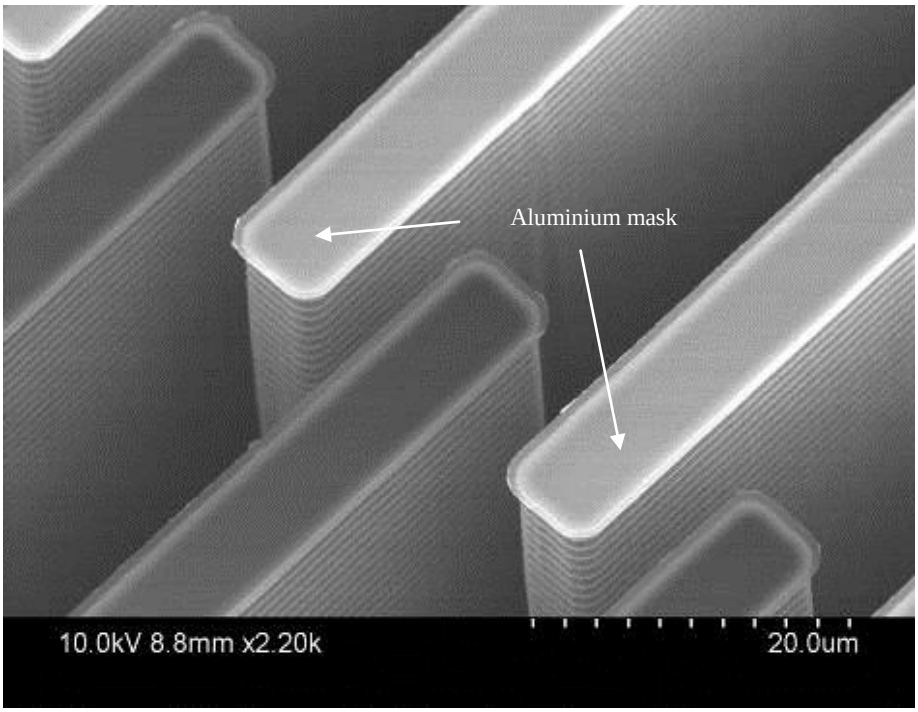

Fig. 4.4. SEM image shows undercutting of comb fingers after DRIE process.

Finally, the stage is experimentally characterized for its modal frequencies. A sinusoidal waveform with frequencies swept for 1 to 1000 Hz is fed from the signal generator (WAVETEK

Model 19) with gain adjusted to maximum output amplitude of 19.3 V to the comb. The amplitude of motion of the end-effector is observed on the microscope (1micron resolution) of the probe station. Fig. 4.5 shows the experimentally observed relationship between frequency and magnitude of vibration. A resonant peak is seen at 811 Hz. This is close to the first dominant frequency predicted by the FEA analysis (at 1120 Hz). The discrepancy observed is due to fabrication imperfections, as the stiffness of the hinges and leaf springs are very sensitive to small dimensional changes in their thickness, which is very close to the fabrication resolution limitation. Also, compared to our previous reports on similar device designs [21, 22], we see a significant broadening of the peak. This could be the result of the viscous thin-film damping in the two additional sensing combs (with large overlap between the fingers, see Fig. 3.2 that have been introduced in this design. The resonance frequency measured by observations with an optical microscope has also been verified by capacitance measurements at the sensing combs.

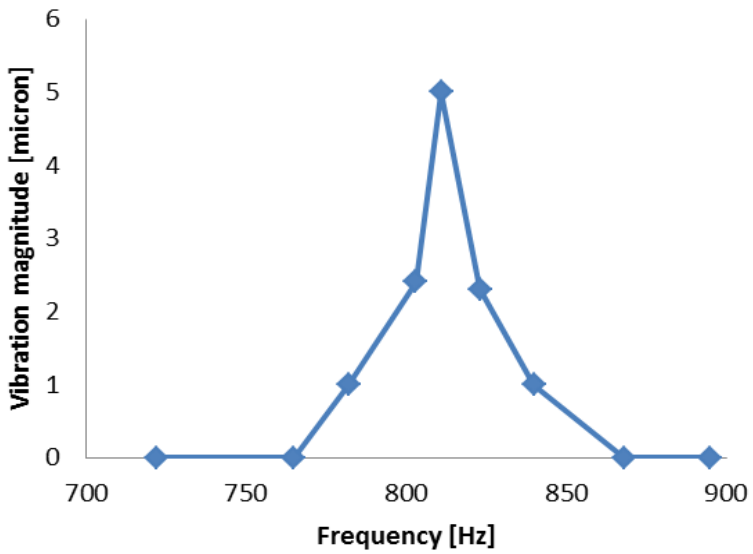

Fig. 4.5. Measured vibration amplitude near resonant frequency with air

CHAPTER 5

RESULTS AND DISCUSSION

5.1 Open-loop response

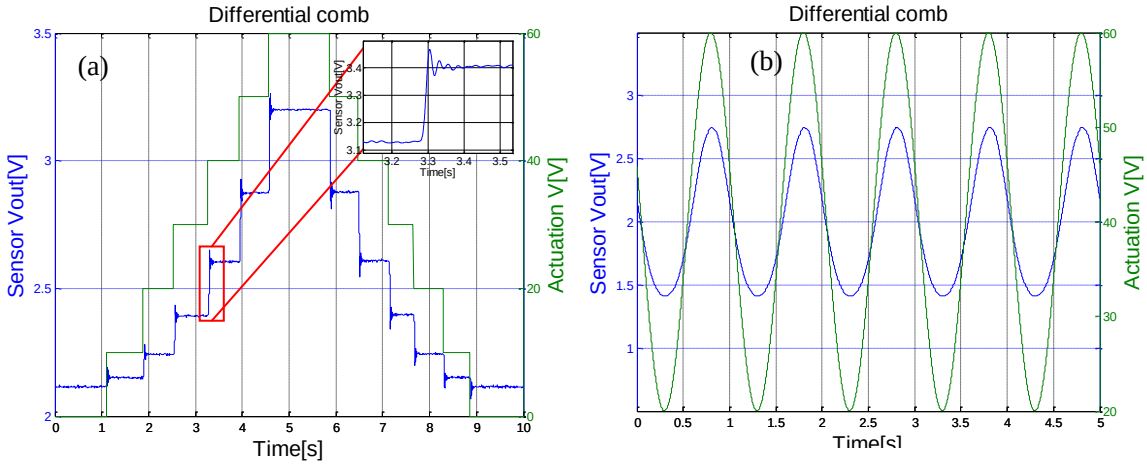

Fig. 5.1. Open-loop response for MEMS XY stage showing the voltage output of capacitance-to-voltage IC and the corresponding actuation voltage for (a) Step input, and (b)

Open loop response results of the system shown in Fig. 5.1 are obtained with both step input and sinusoidal input. As the voltage increases by a fixed amount (10V) in each step, the increment of voltage output from the measurement chip becomes larger at higher actuation voltage as shown in Fig. 5.1(a). This is expected since the electrostatic forces and, hence, displacement of the device is proportional to V^2. The rise time for the system for a step input is approximately 30ms with large overshoot and it's settling time is about 150ms. For sinusoidal command inputs (f = 1Hz), the output can be seen to the square of a sine wave.

5.2 Differential comb drive measurement

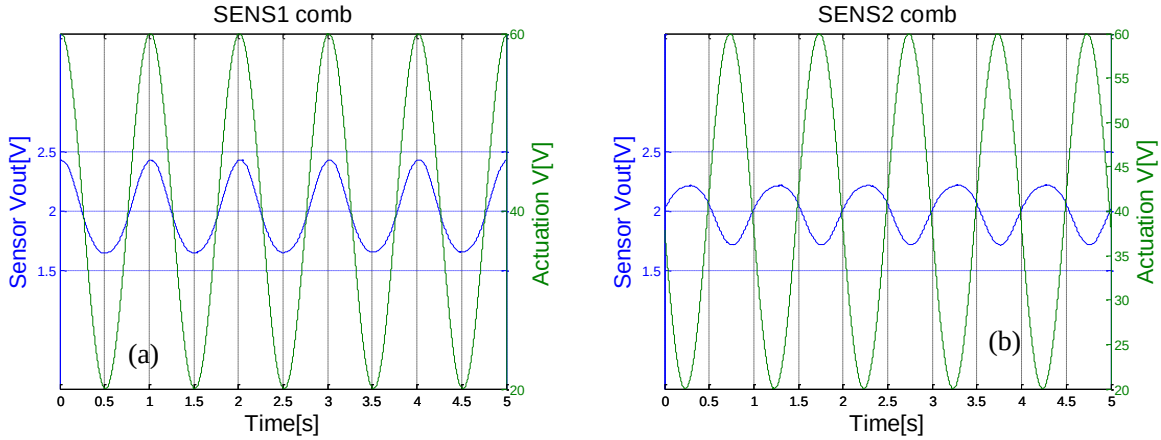

Fig. 5.2. Open-loop response for the MEMS XY stage. (a) Response for sensing comb SENS1; (b) Open-loop response for sensing comb SENS2.

As mentioned in an earlier section, the sensing on each axis consists of two sensing combs, such that when actuated, the capacitance at one comb (SENS1) increases and that at the other (SENS2) decreases. Fig. 5.2(a) and 5.2(b) show the voltage signals output of capacitance-to-voltage conversion IC individually by sensing combs SENSI and SENS2, respectively, when the actuation comb is driven with a sinusoidal actuation voltage having amplitude of 20V and an offset (bias) of 40V. They can be seen to be 180 degrees out of phase. The peak-to-peak change of 0.7906V is obtained in the output voltage signal for SENS1, while that for SENS2 is 0.5082V. This is expected since, because of the design, SENS1 has more fingers than SENS2. When used together in a differential mode, supported by the MS3110 IC, the sensitivity ($\Delta C/\Delta x$) of the system is increased, as indicated by peak-to-peak variation of 1.3353V in the output voltage shown in Fig. 5.1(b).

5.3. Closed-loop response

(a) (b)

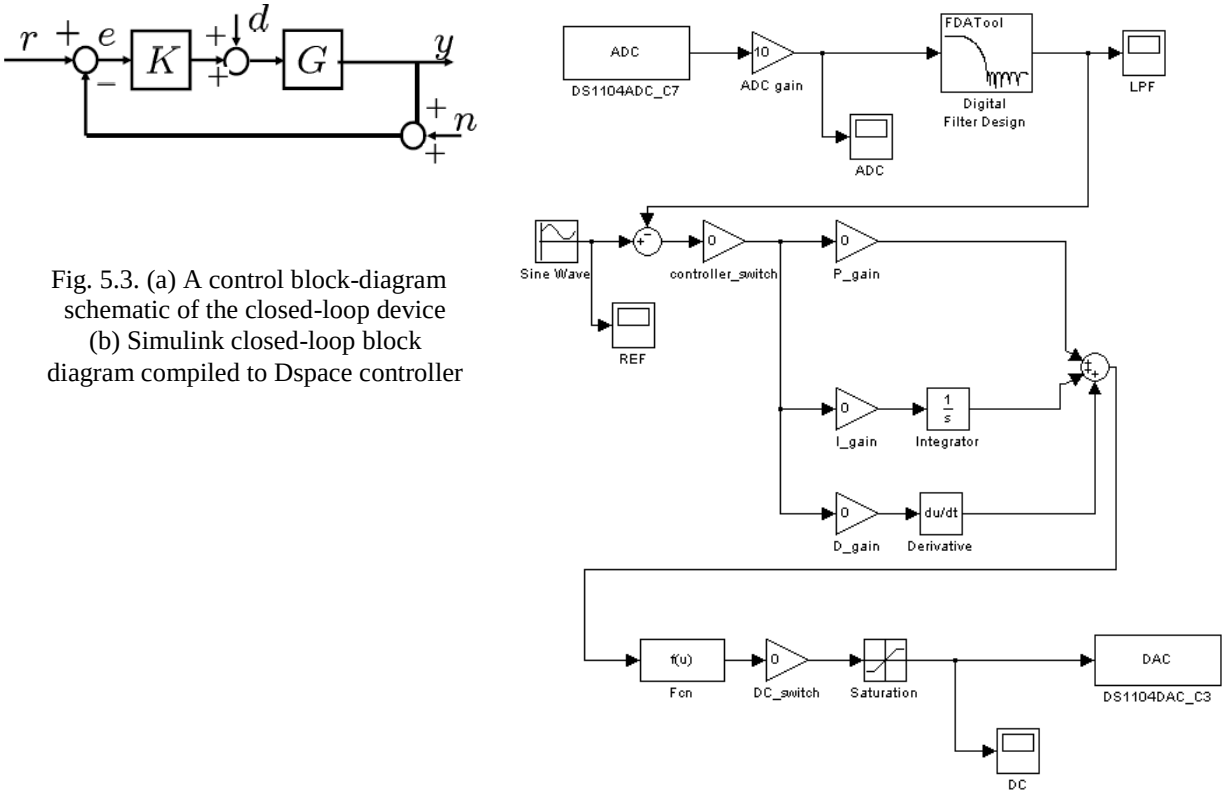

Fig. 5.3. (a) A control block-diagram schematic of the closed-loop device (b) Simulink closed-loop block diagram compiled to Dspace controller

The main use for the sensors that have been introduced into each axis of the stage is that they can be used for feedback-control design. Figure 5.3 represents the feedback control-block diagram of the system. Appropriately designed feedback laws K(s) and their implementations can lead to significant improvements in the positioning bandwidth and resolution, while also enhancing the reliability of the positioning system. In this paper, these improvements are demonstrated by implementation of a PID control design. The PID control law u(t) is given by u(t) = $K_p e(t) + K_i \int_0^t e(\tau) d\tau + K_D \frac{de}{dt}$, (or equivalently K(s) = Kp +Kis + KDs where the proportional, integral, and derivative gains Kp, Ki s, and KD are design parameters. A simple closed-loop PID controller is first implemented for the system using dSPACE's DS1104 platform. Fig. 5.3 (a) and

15(b) shows the closed-loop response of the x-axis (that of the y-axis is essentially the same) to a step input, with the stage operating in ambient conditions.

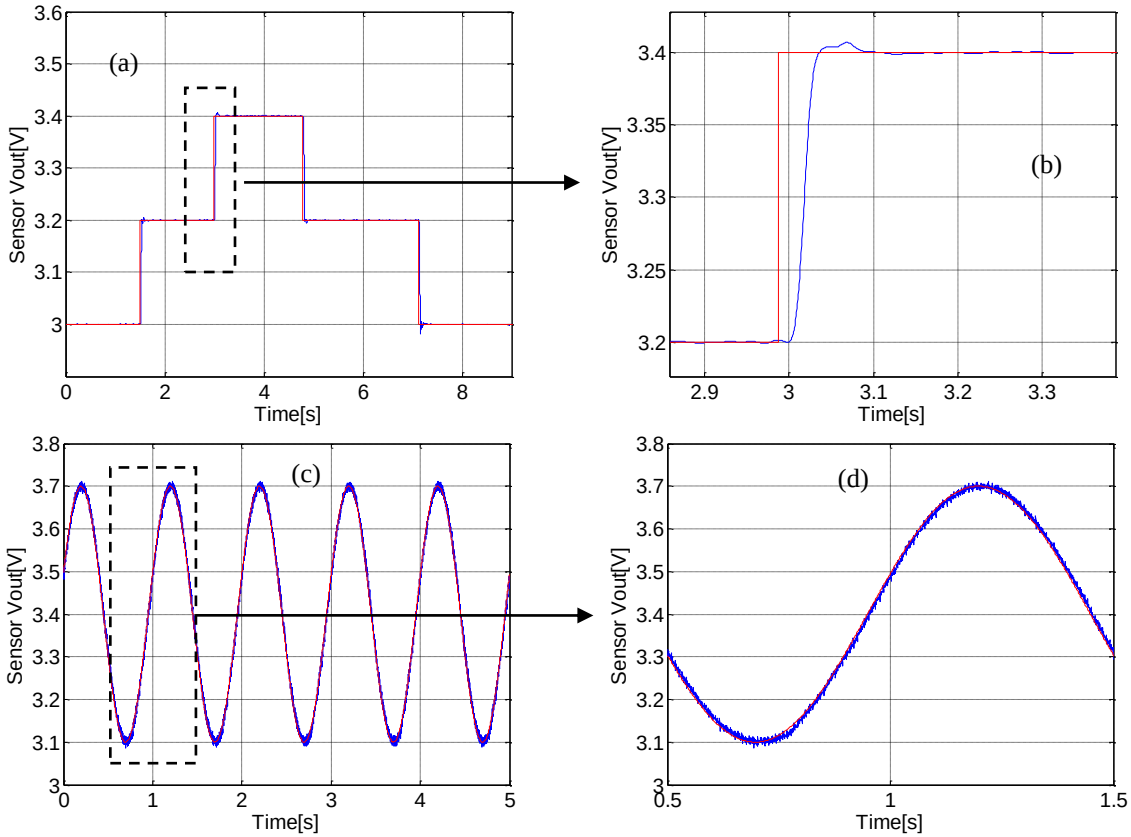

Fig. 5.4. Closed loop response for MEMS XY stage. (a) and (b) : Step reference signal; (c) and (d) : Sinusoidal reference signal

The response suggests a rise time of 50ms and settling time of 100ms. With closed loop position regulation, under ambient conditions, the standard deviation of the feedback signal is observed to be is approximately 3.8916E-4V which corresponds to 5.24nm in terms of positioning. A closed loop bandwidth of approximately 27Hz is achieved. Fig. 15(c) and 15(d) show the x-axis' response to a sinusoidal input (f = 1Hz). A maximum phase lag of 6ms is observed which corresponds to an output lag of 0.008V or 108nm with total motion range of

8μm (corresponding a reference voltage range of 0.6V). With sinusoidal input with higher frequency (f=5Hz), the maximum tracking error increase to 47mV or 633nm.

CHAPTER 6

CONCLUSION

This paper reports on the successful design, fabrication and closed-loop control of a 2 degree-of-freedom, translational (XY) MEMS positioning stage. The device is parallel kinematic mechanism (PKM) to resolve the challenge of designing multi-axis micro stage, with large displacements, low parasitic motion and high mechanical bandwidth. Using standard photolithography and deep reactive ion etching (DRIE), the device can be fabricated on a SOI wafer. The fabricated device has 20μm movement for an actuation voltage of 100V. The device has integrated capacitive sensing as a result of the inclusion of sensing combs into the stage design. These sensing combs produce an experimentally measured sensitivity ($\Delta C/\Delta x$) of around 0.0130pF/μm.

The displacement sensing for the stage is accomplished by sensing the capacitance changes at the sensing combs using a capacitance-to-voltage conversion IC. The system produces voltage signal of around 0.074 V/μm (1.3363 sensor Vout/ 18micron). A rudimentary PID-based closed-loop system was implemented using a commercially available embedded controls platform. The closed loop system has a bandwidth of about 30 Hz and a positioning uncertainty standard deviation of about 5nm. The applications envisioned for this stage include imaging and mechanical characterization of micro and nanostructures such as nanowires, single cells and micro scale tissue samples. Future work will concentrate on the adaptation of this device to these applications. Additionally, closer integration of the sensing circuits with sensing structures is needed to improve the closed-loop tracking performance of the system and fully exploit the mechanical capabilities designed into the positioning stage.

REFERENCES

[1] Li J, Zhang Q X and Liu A Q 2003 Advanced fiber optical switches using deep RIE (DRIE) fabrication *Sensors Actuators* A **102** 286–95

[2] Sun Yu, Nelson B J, Potasek D P and Enikov E A 2002 Bulk microfabricated multi-axis capacitive cellular force sensor using transverse comb drives *J. Micromech. Microeng.* **12** 832–40

[3] Sun Yu, Piyabongkarn D, Sezen A, Nelson B J and Rajamani R 2002 A high-aspect-ratio two-axis electrostatic microactuator ith extended travel range *Sensors Actuators* A **102** 49–60

[4] Indermuehle P F, Linder C, Brugger J, Jaecklin V P and de Rooij N F 1994 Design and fabrication of an overhanging *xy*-microactuator with integrated tip for scanning surface profiling *Sensors Actuators* A **43** 346–50

[5] Indermuhle P-F, Jaecklin V P, Brugger J, Linder C, de Rooij N F and Binggeli M 1995 AFM imaging with an *xy*-micropositioner with integrated tip *Sensors Actuators* A **47** 562–65

[6] Kim C-H, Jeong H-M, Jeon J-U and Kim Y-K 2003 Silicon micro *XY*-stage with a large area shuttle and no-etching holes for SPM-based data storage *J. Microelectromech. Syst.* **12** 470–8

[7] Choi J-J, Park H, Kyu Y K and Jong U J 2001 Electromagnetic micro *x–y* stage with very thick Cu coil for probe-based mass data storage device *Proc. SPIE—Int. Soc. Opt. Eng.***4334** 363–71

[8] Lu Y, Pang C K, Chen J, Zhu H, Yang J P, Mou J Q, Guo G X, Chen B M and Lee T H 2005 Design, fabrication and control of a micro *X–Y* stage with large ultra-thin film recoding media platform *Proc. 2005 IEEE/ASME Int. Conf. on Advanced Intelligent Mechatronics: AIM 2005* pp 19–24

[9] Epitaux M, Verdeil J-M, Petremand Y, Noell W and De Rooij N F 2005 Micro-machined *XY* stage for fiber optics module alignment *IEEE Conf. on Optical Fiber Communication (Anaheim, CA)* pp 131–3

[10] Kim C-H and Kim Y-K 1999 Integration of a micro lens on a micro *XY*-stage *Proc. SPIE— Int. Soc. Opt. Eng.* **3892** 109–17

[11] Kazuhiro T, Ho N K, Kunihiko S, Makoto M, Hiroyuki F and Hiroshi T 2005 A two-dimensional -θ micro optical lens scanner with electrostatic comb-drive *XY*-stage *IEICE Electron. Express* **2** 542–47

[12] Kazuhiro T, Makoto M, Hiroyuki F and Hiroshi T 2006 A high fill-factor comb-driven *XY*-stage with topological layer switch architecture *IEICE Electron. Express* **3** 197–202

[13] Jaecklin V P, Linder C, de Rooij N F, Moret J M, Bischof R and Rudolf F 1992 Novel polysilicon comb actuators for *xy*-stages *Proc IEEE Micro Electro Mech Syst Workshop*pp 147–9

[14] Lee C S B, Han S and MacDonald N C 2000 Single crystal silicon (SCS) *XY*-stage fabricated by DRIE and IR alignment *Proc. IEEE Micro Electro Mechanical Systems(MEMS)* pp 28–33

[15] Kim C-H and Kim Y-K 2002 Micro *XY*-stage using silicon ona glass substrate *J. Micromech. Microeng.* **12** 103–7

[16] Harness T and Syms R R A 2000 Characteristic modes of electrostatic comb-drive *X*-*Y* microactuators *J. Micromech. Microeng.* **10** 7–14

[17] Yao Q, Ferreira P M and Mukhopadhyay D 2005 Development of a novel piezo-driven parallel-kinematics single crystal silicon micropositioning *XY* stage *Proc. SPIE— Int. Soc.Opt. Eng.* **5836** 56–66

[18] Bonev I Delta parallel robot http://www.parallemic.org/Reviews/Review002.html

[19] Yao Q, Dong J and Ferreira P M 2007 Design, analysis, fabrication and testing of a parallel-kinematic micropositioning *XY* stage *Int. J. Mach. Tools Manuf.* **47** 946–61

[20] Yangmin L and Qingsong X 2006 A novel design and analysis of a 2-DOF compliant parallel micromanipulator for nano manipulation *IEEE Trans. Autom. Sci. Eng.* **3** 248–53

[21] Dong J and Ferreira P M, 2009 Electrostatically Actuated Cantilever with SOI-MEMS Parallel Kinematic XY Stage, *IEEE/ASME Journal of Microelectromechanical Systems*, 18(3), 641-651

[22] Dong J, Mukhopadhyay D and Ferreira P M 2007 Design, Fabrication and Testing of Silicon-on-Insulator (SOI) MEMS Parallel Kinematics XY Stage", *Journal of Micromechanics and Microengineering*, 17(6), 1154-1161

[23] Dong J and Ferreira P M 2008 Simultaneous Actuation and Displacement Sensing for Electrostatic Drives", *Journal of Micromechanics and Microengineering*, 18(3), 035011 (10 pp)